

Delay and dispersion characteristics of a frequency-domain optical delay line for scanning interferometry

Andrei V. Zvyagin, Elwyn D. J. Smith, and David D. Sampson

Optical+Biomedical Engineering Laboratory, Department of Electrical and Electronic Engineering, The University of Western Australia, 35 Stirling Highway, Crawley 6009, Western Australia, Australia

Received June 26 2002; revised manuscript received September 4, 2002; accepted September 12, 2002

The reflective frequency-domain optical delay line employing a diffraction grating, a lens, and a tiltable mirror has emerged as a device particularly suitable for interferometry and optical coherence tomography. The device is comprehensively described, both theoretically and experimentally, in the context of interferometry. The variations of phase and group delay produced by the device as well as its dispersive properties are described and demonstrated experimentally. © 2003 Optical Society of America
OCIS codes: 110.4500, 120.3180, 050.5080, 260.2030, 320.5540.

1. INTRODUCTION

Generation of an accurate and rapidly variable optical delay is required in many applications of optics, including optical coherence tomography (OCT) and other forms of scanning interferometry, as well as short-pulse autocorrelators. OCT¹ requires a scanning delay line with linear, millimeter-range optical-path-length variation. Scanning at meter-per-second velocities is required to support image acquisition at video rates. Although many delay lines have been reported, as reviewed by Rollins *et al.*,² few are capable of meeting such demanding specifications.³ To date, the most promising device is the frequency-domain optical delay line (FD-ODL) based on a diffraction grating, a lens, and a tiltable mirror.^{4–6} For convenient operation in a reflection-based interferometer, a folded configuration is generally employed in the delay line. Its operation is based on the time-shifting property of the Fourier transform, i.e., a linear phase ramp in the frequency domain corresponds to a delay in the time domain. The delay line was first applied to OCT in 1997 by Tearney *et al.*,⁶ but its origins go back much further. Apart from scanning group delay, the device may be used to vary dispersion, and, as such, it and a range of close variants have been used in shaping femtosecond and picosecond laser pulses.^{4,7–10} In OCT, variable dispersion is also important. Dispersion balance between reference and sample arms in the interferometer is necessary to achieve the highest possible resolution.⁶

Although there were earlier demonstrations of delay scanning in the context of pulse shaping,¹¹ the device was first demonstrated for the specific purpose of scanning group delay by Kwong *et al.*,⁵ who employed it in a pulse autocorrelator. They achieved approximately linear scans of 2-ps duration (0.6 mm in air) at 400 scans/s.

Tearney *et al.*⁶ achieved highly linear scans over a 3-mm range at 2000 scans/s, equivalent to a velocity of 6 m/s. Tearney *et al.* employed a double-pass configuration to ensure efficient coupling from and to single-mode opti-

cal fibers. Rollins *et al.*² employed a 4-kHz resonant galvanometer-based mirror scanner to further increase the linear scan velocity to 40 m/s, which enabled *in vivo* OCT imaging at video rates. Another advance was the demonstration of the extension of the scan length to 24 mm in air through the incorporation of a double-pass, polarizing reflector.¹² Incorporation of an electro-optic modulator into the delay line to permit high-frequency phase modulation has brought flexibility and is particularly suitable for Doppler OCT.¹³ In a closely related variant, the tiltable mirror was replaced with an acousto-optic deflector,¹⁴ which produced delay scan rates in the many-megahertz range.

For use in OCT, it has been recognized that such delay lines possess several distinctive properties, including the decoupling of the phase and group delay and the control of dispersion.^{2,6} To our knowledge, however, the systematic treatment of such devices as part of a scanning, low-coherence interferometer (as used in OCT) has not been reported. Specifically, this paper considers the FD-ODL employing a diffraction grating, a lens, and a tiltable mirror in a folded configuration. A theoretical model of the operation of the device is presented. The model allows two important characteristics of the optical delay line to be quantified: the variation of phase and group delay and the effect of the group-delay dispersion (GDD) on the evolution of the temporal coherence of light propagating through the device. Experimental results verifying the validity of the model are also reported.

The paper is organized as follows. In Section 2, the theory of operation of the delay line is presented. In Section 3, the experimental setup used to verify the theoretical model is presented. In Section 4, the experimental results are presented and compared with theory. In Section 5, some conclusions are drawn.

2. THEORY

In this section, expressions are derived for the photocurrent at the output of a Michelson interferometer incorpo-

rating the FD-ODL. Ray tracing is used to determine the phase response of the FD-ODL, including the correction required to account for diffraction. An advantage of ray-tracing analysis over the alternative, Fourier transform analysis,⁴ is that the physical origins of all phase shifts are made explicitly clear.

A. Michelson Interferometer and Delay Line

Consider a Michelson interferometer, in which light is split into two paths, as shown schematically in Fig. 1(a). A scanning delay line terminates one path, known as the reference path. The other path is terminated by a sample, with backscatter power reflectivity $R(z)$, where z is the axial coordinate. A light source with broad optical bandwidth and mean wavelength λ_0 is used. The broad bandwidth ensures that coherent interference arising from a single point reflector in the sample is observed over only a small range of axial scanning distance (described by the coherence length l_c , which is typically 10–20 μm for the semiconductor sources commonly used in OCT). The simplest scanning delay line is an axially translated plane mirror. Axial translation by distance Δz in air imparts an additional phase ψ to light, given by $\psi = 4\pi\Delta z/\lambda_0$, which leads to generation of equal phase and group delay.

Consider the FD-ODL shown schematically in Fig. 1(b). A collimated beam is incident on the diffraction grating and dispersed such that the spectral component at λ_0 is diffracted along the optical axis, denoted by z in Fig. 1. A lens with the grating in its front focal plane collimates the dispersed light and projects it onto a tiltable mirror with a pivot point in its back focal plane. The mirror tilt angle θ is assumed small, and the pivot point may be offset from the optical axis by distance x_0 . The tilted mirror causes a phase ramp to be imparted to the spectral components of the beam, which, for small angles, is linearly proportional to θ , as well as a phase offset, which is linearly proportional to θ and x_0 . The reflected, dispersed light is collected by the lens and projected back onto the grating. The grating recollimates the dispersed light into a beam with a range of phase and group delays.

To describe this process, we consider a monochromatic plane wave of wave number k and angular frequency ω , incident on the Michelson interferometer. The electric fields from the sample and reference arms, E_s and E_r , respectively, are represented in scalar form by

$$\begin{aligned} E_s &= E\sqrt{R}\cos[\psi_s(k) - \omega t], \\ E_r &= E\cos[\psi_r(k) - \omega t], \end{aligned} \quad (1)$$

where E is the amplitude and ψ_s and ψ_r are the phases of each wave acquired as a result of the round trip in the sample and reference arms, respectively. The resultant photocurrent, averaged over the photodetector response time, is given by

$$i_d = \phi \frac{R+1}{4} E^2 + \phi \frac{\sqrt{R}}{2} E^2 \cos[\psi_s(k) - \psi_r(k)], \quad (2)$$

where ϕ is the detector responsivity. To evaluate the phases in Eq. (2), we first take into account phase shifts caused by the diffraction grating.

B. Phase Shift from the Diffraction Grating

Ordinarily, the phase ψ of a spectral component at the wave number k is determined by the optical path length nl from $\psi = knl$, where l is the geometric length and n is the refractive index of the medium. (Henceforth, $n = 1$ is assumed for simplicity.) Phases that obey the relation $\psi = knl$ are conventionally termed dynamical¹⁵ and can be evaluated from ray tracing. However, ray tracing alone is insufficient when the optical circuit contains a diffraction element, as can be readily illustrated.

Consider a monochromatic plane wave incident on a grating Gr, as shown schematically in Fig. 2. Points A and B are on the same wave front and thus have equal phase, and similarly for points B and C. However, consideration of the path lengths of rays 1 and 2 incorrectly suggests that ray 2 acquires an additional phase shift corresponding to the path AOC . The inadequacy of ray tracing was first noted by Treacy,⁷ who introduced a phase correction term in order to apply it to temporal pulse analysis. Martinez *et al.*⁸ extended Treacy's analysis to include refractive elements. In the present case, it is anticipated that a correction term equivalent to the path AOC should be found. It is shown in Appendix A that a ray diffracted at point B on the grating acquires an

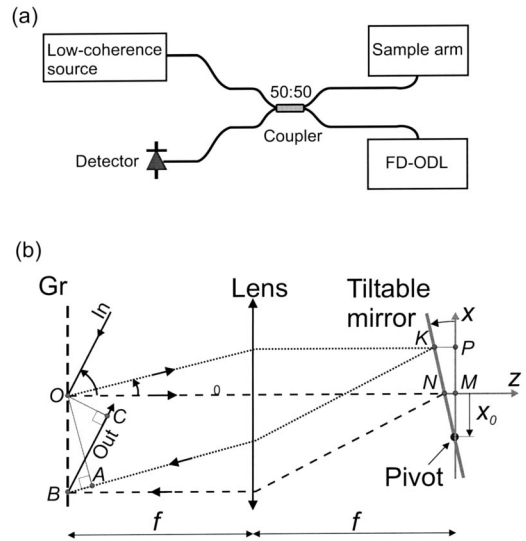


Fig. 1. Schematic diagrams of (a) scanning Michelson interferometer employing the frequency-domain optical delay line (FD-ODL) and (b) FD-ODL.

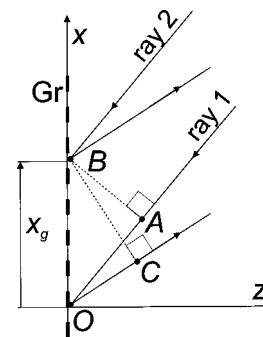


Fig. 2. Ray representation of plane-wave diffraction from a diffraction grating (Gr).

additional phase ψ^{corr} compared with that of a ray diffracted at point O, which is given by

$$\psi^{\text{corr}}(x_g) = k_g m x_g, \quad (3)$$

where $k_g = 2\pi/p$, p is the grating period, m is the diffraction order, and x_g is the geometric length of path OB . The phase $\psi(k, x)$ at a given location x , with respect to the reference point at the origin, is thus given by

$$\psi(k, x) = \psi^{\text{dyn}}(k, x) + \psi^{\text{corr}}(x), \quad (4)$$

where $\psi^{\text{dyn}}(k, x)$ represents the dynamical phase, found through ray tracing. The correction term $k_g m x_g$ exactly matches the dynamical phase accumulated over the path AOC but with opposite sign. Hence the optical phases at A, B, and C are identical, as anticipated.

C. Phase Shifts in the Frequency-Domain Optical Delay Line

To derive the phase of a wave after one round trip through the FD-ODL, we consider the difference $\Delta\psi_D(k, \theta)$ between the phase acquired by a ray of arbitrary wave number k when θ is nonzero and the phase acquired when $\theta=0$, i.e.,

$$\Delta\psi_D(k, \theta) = \psi_D(k, \theta) - \psi_D(k, 0). \quad (5)$$

In Eq. (5), the dependent variable θ is used in preference to x , which is acceptable, since they are linearly related. Using Eq. (4), we may rewrite Eq. (5) as

$$\begin{aligned} \Delta\psi_D(k, \theta) &= [\psi_D^{\text{dyn}}(k, \theta) - \psi_D^{\text{dyn}}(k, 0)] \\ &\quad + [\psi^{\text{corr}}(\theta) - \psi^{\text{corr}}(0)] \\ &= \Delta\psi_D^{\text{dyn}}(k, \theta) + \psi^{\text{corr}}(\theta), \end{aligned} \quad (6)$$

where the phase correction term on axis $\psi^{\text{corr}}(0)$ is equal to zero. The phase difference $\Delta\psi_D^{\text{dyn}}(k, \theta)$ may be calculated based on the following observations. With reference to Fig. 1, geometric path length is denoted by capital letters, e.g., OK , and optical path length is denoted $[OK]$.

1. For a polychromatic beam, rays diverging from the grating at point O recombine at point B on the grating and exit the delay line along the single ray BC .

2. For evaluation of $\Delta\psi_D^{\text{dyn}}(k, \theta)$, it is sufficient to compare optical paths of the rays of wave number k with nonzero θ and zero θ from their common point of incidence at O, through the delay line and reincident on the grating, to points C and O, respectively. From points C and O, the phase difference between these rays is constant.

3. $\psi_D^{\text{dyn}}(k, \theta)$ is obtained from the corresponding ray path $[OKBC]$.

4. The round-trip optical path between the grating and the mirror is invariant for all spectral components. In particular, when $\theta=0$, the round-trip path becomes $[OMO]$. Similarly, the optical path $[OKB]$ for a ray corresponding to a redshifted spectral component $\lambda > \lambda_0$ is equal to the optical path $[ONB]$ corresponding to the mean spectral component λ_0 .

5. The mirror tilt generates identical optical path variation for all spectral components, which is simply evaluated from the path followed by λ_0 : $[ONB] - [OMO] = 2MN$.

The dynamical phase variation in the delay line is thus given by

$$\Delta\psi_D^{\text{dyn}}(k, \theta) = k(2MN + BC) = 2kx_0\theta + kBC. \quad (7)$$

The signs of θ , α , and β , which are defined as shown in Fig. 1, are positive for counterclockwise rotation, and, for the configuration shown, x_0 and MN are negative, whereas m and BC are positive. It follows from the grating equation, given by

$$p(\sin\alpha + \sin\beta) = m\lambda, \quad (8)$$

that

$$k(BC + AB) = -k_g m OB, \quad (9)$$

where OB is negative, as drawn in Fig. 1. When we combine Eqs. (6)–(9) and use Eq. (3), the total phase variation is

$$\Delta\psi_D(k, \theta) = 2kx_0\theta - kAB, \quad (10)$$

and noting that $AB = 2\theta f \sin\beta$, we obtain

$$\Delta\psi_D(k, \theta) = 2kx_0\theta - 2k\theta f \sin\beta. \quad (11)$$

With the λ_0 ray directed along the z axis, the grating equation requires that

$$p \sin\beta = m(\lambda - \lambda_0), \quad (12)$$

and substitution into Eq. (11) gives

$$\Delta\psi_D(k) = 2kx_0\theta + \frac{4\pi m \theta f (k - k_0)}{pk_0}, \quad (13)$$

where $k_0 = 2\pi/\lambda_0$. After the phase change at the grating is accounted for, Eq. (13) arises directly from the geometric path length $2MN - AB$. This geometric length is approximately equal to twice the axial shift in mirror position, $2PK$, in the small-angle approximation for β . This approximation was used by Kwong *et al.*⁵ to obtain a similar result when the grating is tilted. However, use of this approximation can be misleading, since it is not obvious that it accounts for the geometric-path-length changes and diffraction at the grating. (The case of a tilted grating is treated in Subsection 2.E.)

The corresponding expression in Rollins *et al.*² is twice that of Eq. (13), since the authors considered two passes through the system. The sign of the second term is opposite, and m does not appear. With regard to the group-delay expression and the diagram in Rollins *et al.*, the mirror angle and offset used there have signs opposite to those of θ and x_0 as defined in this paper, and the diffraction order $m = +1$, and hence Eq. (13) above is in agreement with Eq. (11) in Rollins *et al.* Note that for exact equality between Eqs. (11) and (12) in Rollins *et al.*, the angular frequency appearing in the denominator of Eq. (12) should be the mean angular frequency.

The corresponding expression in Tearney *et al.*⁶ is equivalent to Eq. (13) for a normal grating in the small-angle approximation, assuming that the diffraction order $m = +1$, although the actual diffraction order m does not appear in their phase expression and cannot be unambiguously determined from their diagram.

D. Interferometer Output

The phases of waves completing a round trip in the sample and reference arms are given by $\psi_s(k) = 2kL_s$ and $\psi_r(k) = 2kL_r + \Delta\psi_D(k)$, respectively, where L_s is the optical path length in the sample arm. L_r is the optical path length in the reference arm, including the contribution from the FD-ODL at the operating point $\theta=0$. Substituting these expressions and Eq. (13) into Eq. (2) and neglecting the direct-current component gives

$$\begin{aligned} i_d(k) &= \phi \frac{\sqrt{R}}{2} E^2 \cos[2k(L_r - L_s) + \Delta\psi_D(k)] \\ &= \phi \frac{\sqrt{R}}{2} E^2 \cos[\psi(k)], \end{aligned} \quad (14)$$

with

$$\psi(k) = 2k\delta + 2kx_0\theta + \frac{4\pi m\theta f(k - k_0)}{pk_0}, \quad (15)$$

where $\delta = L_r - L_s$ is equivalent to the conventional optical-path-length mismatch in the interferometer. The photocurrent i_d under broadband illumination is found from

$$\begin{aligned} i &= \int_0^\infty i_d(k)G(k)dk \\ &= \phi \frac{\sqrt{R}}{2} E^2 \operatorname{Re} \left\{ \int_0^\infty G(k) \exp[j\psi(k)] dk \right\}, \end{aligned} \quad (16)$$

where $G(k)$ is the power spectral density of the light source, which is assumed to be unmodified by the interferometer. The phase shift $\psi(k)$ can be represented by a Taylor series about k_0 , given by

$$\begin{aligned} \psi(k) &= \psi(k_0) + \psi'(k_0)(k - k_0) + \psi''(k_0) \frac{(k - k_0)^2}{2!} \\ &\quad + \psi'''(k_0) \frac{(k - k_0)^3}{3!} + \dots, \end{aligned} \quad (17)$$

where a prime denotes differentiation with respect to k . The first and second terms in Eq. (17) determine the phase and group delays, respectively. When we compare Eqs. (15) and (17), the phase delay t_p and the group delay t_g are found to be

$$t_p = \frac{1}{c} \frac{\psi(k_0)}{k_0} = \frac{2\delta}{c} + \frac{2\theta x_0}{c}, \quad (18)$$

$$t_g = \frac{1}{c} \psi'(k_0) = \frac{L_g}{c} = \frac{2\delta}{c} + \frac{2\theta x_0}{c} + \frac{4\pi m\theta f}{cpk_0}, \quad (19)$$

respectively, where c denotes the speed of light in vacuum and L_g is the group-delay length. Equations (18) and (19) show that the phase and group delays are not constrained to be equal and can be separately altered by choice of the parameters of the delay line. It is convenient to characterize the phase/group delay behavior in terms of the interferogram modulation index ξ , defined as the ratio of phase and group delays for a path-matched interferometer, i.e., when $\delta=0$, and given by

$$\xi \equiv \left. \frac{t_p}{t_g} \right|_{\delta=0} = \left(1 + \frac{m\lambda_0 f}{px_0} \right)^{-1}. \quad (20)$$

The magnitude of ξ is interpreted as the ratio of the number of fringes within the envelope to the number of fringes that would be present in an interferogram obtained for equal phase and group delay, as when translating a mirror. If ξ is negative, variation in θ causes the fringes and the envelope to shift in opposite directions. Figure 3 shows a plot of ξ versus offset x_0 .¹⁶ Three representative regimes of operation are indicated: A, the normally modulated regime, where t_g asymptotically approaches t_p ($\xi \rightarrow 1$ as $x_0 \rightarrow \pm\infty$), and hence the interferogram approaches that obtained from a translating-mirror scanning interferometer; B, the fully demodulated regime, for which $t_p = 0$ and $t_g \neq 0$, attained when $x_0 = 0$; and C, the achromatic regime, for which $t_g = 0$ and $t_p \neq 0$. An achromatic phase shift is attained when $t_g = 0$, which requires that

$$x_0 = -\frac{m\lambda_0 f}{p}. \quad (21)$$

As shown by Eq. (6), the spectral phase generated by the FD-ODL is the sum of a dynamical term and an achromatic correction term. Zero group delay requires that the optical path length for λ_0 not change with θ , and hence the corresponding dynamical term becomes zero, leaving only the achromatic term. For this to occur, lengths $2MN$ and BC in Fig. 1 must be equal and opposite [cf. Eq. (7)], and this does indeed hold when Eq. (21) is satisfied, provided that θ is small.

E. Dispersion

Group-delay dispersion (GDD) is defined as $D_\omega \equiv d^2\psi/d\omega^2|_{\omega=\omega_0} = \psi''(k_0)/c^2$, and second-order GDD, or differential dispersion, is defined as $D_\omega^{(1)} \equiv d^3\psi/d\omega^3|_{\omega=\omega_0} = \psi'''(k_0)/c^3$. Note that D_ω and $D_\omega^{(1)}$ are sometimes referred to as second- and third-order dispersion, respectively. As configured in Fig. 1, the delay line is dispersion free. However, alterations from the ideal configuration, including grating translation or tilt and lens aberrations, give rise to nonzero dispersion, in gen-

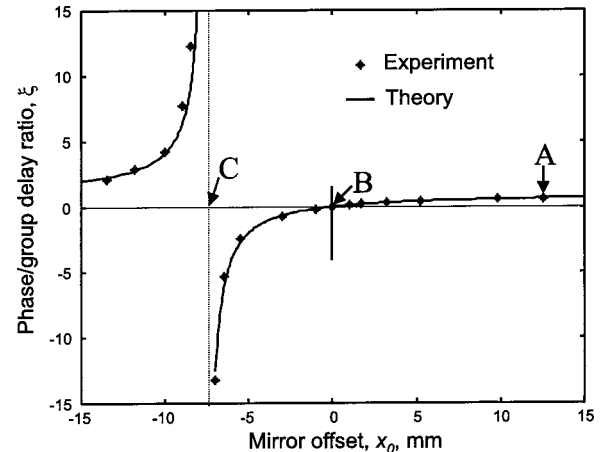


Fig. 3. Plot of phase-to-group-delay ratio ξ versus mirror offset x_0 . Points A, B, and C denote three regimes of interest.

An equivalent expression to Eq. (31), with the substitution $m = +1$, appears in Tearney *et al.*⁶ Performing a Taylor-series expansion of Eq. (31) leads to the first-order approximation

$$\Delta\psi_D(k) \approx 2kx_0\theta + \frac{4\pi\theta f m(k - k_0)}{pk_0 \cos\theta_g}, \quad (32)$$

and the higher-order dispersive terms result in Eqs. (29) and (30), where we substitute $\Delta z = f\theta \tan\theta_g$. Hence mirror-tilt-dependent dispersion is produced when $\theta_g \neq 0$. Consequently, a tilted grating allows linearly delay-dependent dispersion variation, which may be useful for dispersion matching to dispersive samples, for example. Note that relation (32) can be simply obtained from Eq. (11) by using the small- β approximation $p \cos\theta_g \sin\beta \approx m(\lambda - \lambda_0)$, which is how an expression equivalent to relation (32) with $x_0 = 0$ and $m = -1$ was obtained by Kwong *et al.*⁵

In Section 3, the experimental setups used to confirm the theoretical predictions are described.

3. EXPERIMENT

Measurements were performed by using two setups similar to that shown schematically in Fig. 1. In the first setup, light from a superluminescent diode with near-Gaussian power spectral density centered at 843 nm with 20-nm bandwidth was incident on a bulk-optic Michelson interferometer. The FD-ODL employed a grating with 830 lines/mm and an achromatic doublet lens with 60-mm focal length. A galvanometer with a 30-mm-wide mirror and a maximum scan rate of 1 kHz provided the tilt scanning, and a double pass through the delay line (not shown in Fig. 1) was performed as described elsewhere.¹²

The second setup was designed to access the so-called achromatic regime. As seen from Eq. (21), to keep the offset distance to a value accessible by a galvanometer mirror, it is convenient to reduce the wavelength of operation and the focal length of the lens and to decrease the period of the grating. Hence, in this setup, a laser diode operating below threshold with near-Gaussian spectral density centered at 635 nm with 11-nm bandwidth, a transmission grating with 300 lines/mm, and an achromatic doublet lens with 40-mm focal length were employed. The transmission grating required the incident light to approach from the left-hand side of the grating plane shown in Fig. 1, and a single-pass configuration was chosen because of the low diffraction efficiency of the grating.

4. RESULTS

The key parameters determining the behavior of the FD-ODL are mirror tilt angle θ , pivot offset x_0 , interferometer path-length mismatch δ , GDD D_ω , and differential dispersion $D_\omega^{(1)}$. In this section, the different regimes of operation arising from these parameters are highlighted, and theoretical predictions are confirmed with experimental results. Interferograms, i.e., measurements of i versus θ or, equivalently, i versus scanning distance, calculated by means of Eqs. (22)–(25), are presented.

A. Zero Mirror Offset ($x_0 = 0$)

We begin by considering the zero-dispersion case. Figure 5 shows several measured interferograms corresponding to $x_0 = 0$ over a range of path mismatches δ . The path mismatch slowly varied between measurements as a result of environmental fluctuations. The uppermost curve in Fig. 5 corresponds to the case $\delta \cong 0$. The theoretical curve is shown as dashed, and it is calculated by inserting the experimental parameter values into Eq. (25). The lowermost curve corresponds to the case $2k_0\delta \cong \pi$. The cases $2k_0\delta = \pm\pi/2$ theoretically give zero signal, a measured example of which is seen in Fig. 5. The other curves in Fig. 5 represent intermediate values of $2k_0\delta$. Based on Eq. (22) with $x_0 = D_\omega = D_\omega^{(1)} = 0$, each interferogram should have the same shape in θ , as confirmed by Fig. 5.

The interferograms arising for zero offset are termed “fully demodulated,” since no fringes appear within their envelopes. If the environmental phase fluctuations are assumed to be uniformly random, then the envelope amplitude near the maximum or minimum value has the greatest likelihood of occurring, with the zero-amplitude case being least likely, and therefore the envelope is most commonly observed experimentally to “flip” between extrema. In many applications, e.g., low-coherence interferometry,¹⁸ the desired signal is the envelope of an interferogram. However, such a fully demodulated interferogram is not useful for envelope detection, since, as shown in Eq. (25) and seen in Fig. 5, the envelope amplitude is dependent on optical phase fluctuations. If further independent phase modulation is applied, however, a useful envelope detection system may still result.¹³

B. Finite Mirror Offset ($x_0 \neq 0$)

For $x_0 \neq 0$, modulation is introduced into the interferogram signal, since the phase varies linearly with θ . If x_0 is large, then one expects many fringes in the interferogram, as in the interferogram of a translating-mirror scanning interferometer. If x_0 is small, the difference from the case $x_0 = 0$ may not be apparent when the interferogram is at its maximum or minimum, but this dif-

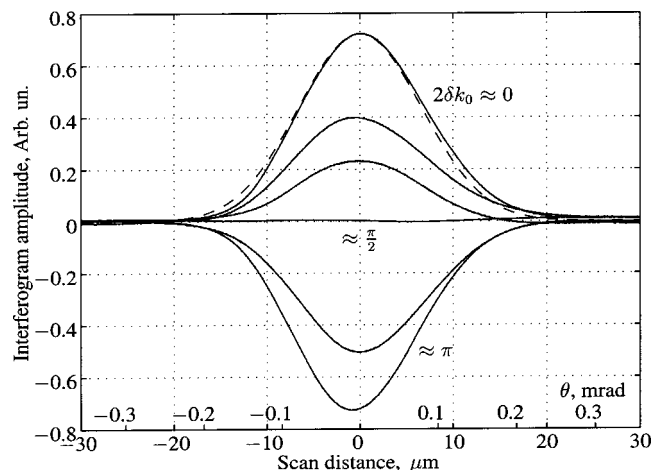


Fig. 5. Interferograms for zero pivot offset plotted versus mirror tilt angle and the corresponding axial scan distance. Solid curves represent experimental results, and the dashed curve is the theoretical envelope.

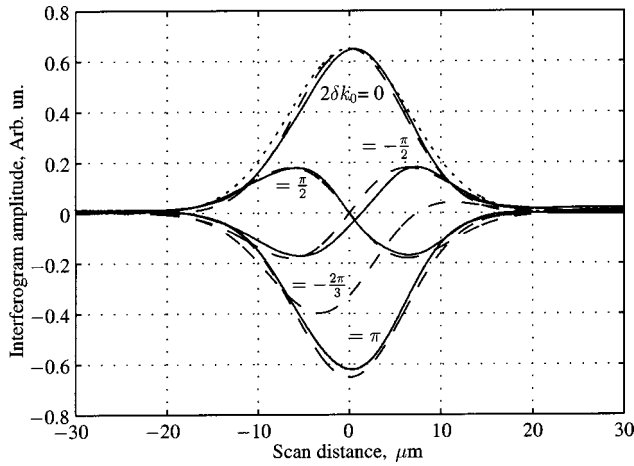


Fig. 6. Interferograms for small pivot offset plotted versus axial scan distance. Solid and dashed curves represent experimental and theoretical results, respectively (with the use of $2\delta k_0$ values as shown, where $x_0 = 200 \mu\text{m}$). The dotted curves represents the calculated interferogram envelope.

ference becomes clearly visible as path lengths fluctuate, since the interferogram cannot be completely zero (for all θ), as in the $x_0 = 0$ case. This effect can be clearly seen in Fig. 6, in which the measured interferograms correspond approximately to phase shifts $2k_0\delta = 0, \pi/2, -\pi/2,$ and π for the case $x_0 = 200 \mu\text{m}$. The dashed curves in Fig. 6 are calculated by using Eq. (25) and correspond closely with the measurements. The calculated trace for $2k_0\delta = -2\pi/3$ is also shown to indicate the intermediate behavior. In general, if the interferometer phase $2k_0\delta$ is such that the cosine term in Eq. (25) is zero when θ corresponds to the middle of the Gaussian envelope, then the interferogram must have odd symmetry. Hence any observed deviation from odd symmetry when the interferogram is zero at the envelope midpoint indicates that other effects such as dispersion must be present, and this is considered in Subsection 4.D.

C. Finite Offset $x_0 = -m\lambda_0/f/p$: Achromatic Regime

An experimental determination of ξ was made for various values of the mirror offset by counting the number of fringes within the interferogram envelope. The fringe count was then normalized to the number of fringes in the translating-mirror interferogram, which was determined separately. The experimental points are plotted in Fig. 3 and show excellent agreement with the theoretical curve. Figure 7 shows measured interferograms¹⁶ employing the second setup described in Section 3 and corresponding to the three regimes of interest indicated in Fig. 3. These interferograms were each recorded over the same time interval of 20 ms, corresponding to an angular scan range of 25 mrad. The interferograms have been normalized to cancel out the slight (approximately 20%) variation in visibility of the Michelson interferometer over the tilt range. This variation was caused by lateral walk-off of the reference beam in the output path of the interferometer and was observed for all three regimes. Operation at point A corresponded to a scan range of 1 mm in air. Point B corresponds to full optical demodulation of the interferogram, which produces only the envelope, as described

above. Point C corresponds to the achromatic regime, in which the envelope of the interferogram is essentially constant over a full scan of the tilt angle.

D. Finite Dispersion

Both small- and large-dispersion regimes were investigated experimentally for $x_0 = 0$. The effect of small dispersion is illustrated in Fig. 8. The experimental traces were obtained after translating the grating away from the lens by $\Delta z = 280 \mu\text{m}$ compared with the position used in generating the data for Fig. 5. This translation corresponds, as a result of Eq. (29) and doubling due to the double-pass configuration, to the condition $D_\omega \rho^2 = -0.42$, which was used in Eq. (24) to calculate the curves shown as dashed in the figure.

Differential dispersion is neglected in Eq. (24). If, in addition, it is assumed that D_ω does not depend on θ , as is the case for an axial grating displacement, then the phase term in Eq. (24) is purely an even function of θ through the L_g^2 term. Hence if the mirror offset is zero, the interferogram will have even symmetry, regardless of the

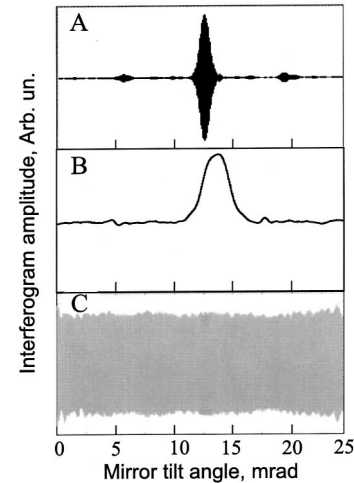


Fig. 7. Interferograms versus mirror tilt angle measured at mirror offsets denoted by points A, B, and C in Fig. 3.

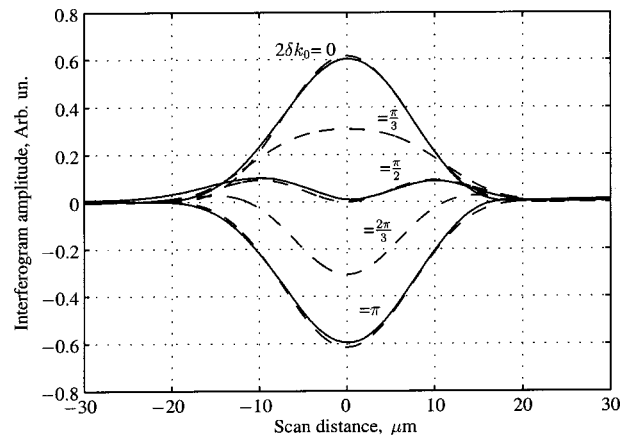


Fig. 8. Interferograms for zero pivot offset and small dispersion plotted versus axial scan distance. Solid and dashed curves represent experimental and theoretical results, respectively (with the use of $2\delta k_0$ values as shown, where $x_0 = 0$ and $D_\omega \rho^2 = -0.42$).

interferometer phase drift. This is a useful diagnostic tool, particularly when only a small amount of dispersion is present in the system.

When the dispersion is small and the interferogram is at a maximum, comparison of Figs. 5 and 8 shows that it is barely distinguishable from the interferogram expected without any dispersion. However, even small amounts of dispersion become clearly visible as the phase fluctuates, especially to the point where the interferogram is zero at the envelope midpoint, since the rest of the interferogram cannot also be zero, and it should have even symmetry. It can be seen that the measured trace corresponding to $2k_0\delta = \pi/2$ in Fig. 8 does not have perfect even symmetry, and hence the conditions of constant D_ω , $x_0 = 0$, and $D_\omega^{(1)} = 0$ were not exactly satisfied in our experimental configuration, since such departures each lead to phase terms with odd symmetry. It is likely that this departure is caused by nonnegligible differential dispersion, which arose because of the imperfect dispersion balance of the different optical elements required in each interferometer arm.

Figure 9 shows the interferogram resulting from a large amount of dispersion ($D_\omega\rho^2 = -7.5$), introduced by moving the grating by 5 mm. The interferogram envelope is now significantly broadened by this dispersion, and the dominant quadratic phase variation can be clearly seen. The interferogram is not completely symmetric, again indicating residual mirror pivot offset or differential dispersion, and, indeed, the interferogram shown by a dashed curve in Fig. 9 has been calculated by using Eq. (24), with $D_\omega\rho^2 = -7.5$ and $x_0 = 0$, and a value of $D_\omega^{(1)} = -410 \text{ fs}^3$ was chosen to best fit the measured data. Experimentally, it was not possible to obtain a completely symmetric interferogram. This highlights the fact that the differential and group-delay dispersion terms due to grating displacement are not independent [cf. Eqs. (29) and (30)]. Therefore, in general, it is not possible to compensate fully for dispersion imbalance elsewhere in the interferometer simply by moving the grating in an FD-ODL, although this may achieve sufficient performance for many purposes. Recently, we have confirmed experimentally the delay-dependent dispersion

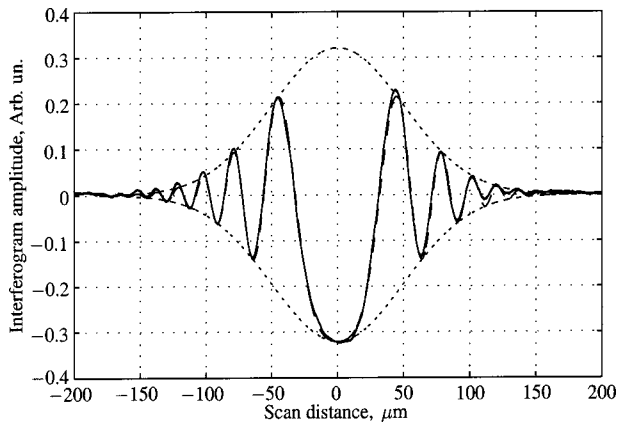


Fig. 9. Interferograms for zero pivot offset and large dispersion plotted versus axial scan distance. Solid and dashed curves represent experimental and theoretical results, respectively (with the use of $x_0 = 0$ and $D_\omega\rho^2 = -7.5$). The dotted curve represents the calculated interferogram envelope.

variation when the grating is tilted and have used this to demonstrate real-time, depth-dependent dispersion compensation in a scanning interferometer.¹⁹

5. DISCUSSION AND CONCLUSION

The primary assumptions made in the analysis presented here are that the lens is ideal and that the mirror tilt θ is small. Under these assumptions, the maximum attainable delay range in a double-pass configuration is given approximately by $L_g^{\max} \cong A\lambda_0/p$, where A is the aperture of the lens. However, large mirror tilt and/or large mirror pivot offset mean that the tiltable mirror is farther from the focal plane, and this departure, together with real lens aberrations, may lead to significant unwanted beam deviation and dispersion variation. Consequently, attention to the optical design is expected to be important in order to minimize unwanted dispersion variation and to maximize the scanning range available without introducing excessive losses, particularly for coupling the output into a single-mode fiber. Grating diffraction efficiency is significantly polarization sensitive; hence single-polarization implementations are usually preferable to minimize the resulting power loss. As the optical bandwidth is increased, the necessary apertures are increased, posing further optical design challenges, and the wavelength sensitivity of the diffraction efficiency also introduces practical limitations. Nonetheless, the frequency-domain optical delay line is a useful and versatile device, allowing rapid phase- and group-delay scanning, together with simple adjustment of both fixed and depth-dependent dispersion. Its application in various forms in scanning interferometry and in optical coherence tomography is expected to increase as its advantages become more widely known.

APPENDIX A: PHASE CORRECTION DUE TO DIFFRACTION

Consider a monochromatic, linearly polarized plane wave with wave vector $\mathbf{k}^{(i)} = (k_x^{(i)}, 0, -k_z^{(i)})$, where $|\mathbf{k}^{(i)}| = k$, incident on a grating situated in the x - y plane, as shown in Fig. 2. The complex electric field of the incident wave can be expressed as

$$\mathbf{E}^{(i)}(x, z) = \mathbf{E}_0^{(i)} \exp[j(k_x^{(i)}x - k_z^{(i)}z - \omega t)], \quad (\text{A1})$$

where (i) denotes incident and $\mathbf{E}_0^{(i)}$ is the amplitude. Using Maxwell's equations with periodic surface boundary conditions, we may apply a Rayleigh expansion to the diffracted field,²⁰ which is then expressed as a sum of plane waves with wave vector $\mathbf{k}_m^{(d)} = (k_{m,x}^{(d)}, 0, k_{m,z}^{(d)})$, given by

$$\mathbf{E}^{(d)}(x, z) = \sum_{m=-\infty}^{+\infty} \mathbf{E}_{m,0}^{(d)} \exp[j(k_{m,x}^{(d)}x + k_{m,z}^{(d)}z - \omega t)], \quad (\text{A2})$$

where (d) denotes diffracted, $|\mathbf{k}_m^{(d)}| = k$, and $|\mathbf{E}_{m,0}^{(d)}|$ is the amplitude of the m th-order diffracted field. Each diffracted order m is characterized by a wave vector projected onto the x axis of the grating, $k_{m,x}^{(d)}$, given by²¹

$$k_{m,x}^{(d)} = k_{m,x}^{(i)} + mk_g. \quad (\text{A3})$$

In most cases, only one diffracted order m is of interest, for which Eq. (A2) is reduced to

$$\mathbf{E}_m^{(d)}(x, z) = \mathbf{E}_{m,0}^{(d)} \exp(j\{(k_{m,x}^{(i)} + mk_g)x + [k^2 - (k_{m,x}^{(i)} + mk_g)^2]^{1/2}z - \omega t\}). \quad (\text{A4})$$

Comparison of the incident and diffracted fields on the surface of the grating, i.e., setting $z = 0$ in Eqs. (A1) and (A4), respectively, reveals a phase difference given by $mk_g x_g$, where x_g is the distance from a reference location on the grating. Note that m and x_g are positive in the configuration shown in Fig. 2. Hence, in the framework of ray optics and with reference to Fig. 2, a ray diffracted at point B on the grating acquires an additional phase ψ^{corr} compared with that of a ray diffracted at a reference point O, given by

$$\psi^{\text{corr}}(x_g) = k_g m x_g. \quad (\text{A5})$$

ACKNOWLEDGMENT

We acknowledge Simon Moore for useful and stimulating discussions during the preparation of this manuscript.

Corresponding author Andrei V. Zvyagin's e-mail address is: azvyagin@ee.uwa.edu.au.

REFERENCES AND NOTES

1. D. Huang, E. A. Swanson, C. P. Lin, J. S. Schuman, W. G. Stinson, W. Chang, M. R. Hee, T. Flotte, K. Gregory, C. A. Pulifito, and J. G. Fujimoto, "Optical coherence tomography," *Science* **254**, 1178–1181 (1991).
2. A. M. Rollins, M. D. Kulkarni, S. Yazdanafar, R. Ungarunyawee, and J. A. Izatt, "In vivo video rate optical coherence tomography," *Opt. Express* **3**, 219–229 (1998); <http://www.opticsexpress.org>.
3. G. J. Tearney, B. E. Bouma, S. A. Boppart, B. Golubovic, E. A. Swanson, and J. G. Fujimoto, "Rapid acquisition of *in vivo* biological images by use of optical coherence tomography," *Opt. Lett.* **21**, 1408–1410 (1996).
4. R. N. Thurston, J. P. Heritage, A. M. Weiner, and W. J. Tomlinson, "Analysis of picosecond pulse shape synthesis by spectral masking in a grating pulse compressor," *IEEE J. Quantum Electron.* **QE-22**, 682–696 (1986).
5. K. F. Kwong, D. Yankelevich, K. C. Chu, J. P. Heritage, and A. Dienes, "400-Hz mechanical scanning optical delay line," *Opt. Lett.* **18**, 558–560 (1993).
6. G. J. Tearney, B. E. Bouma, and J. G. Fujimoto, "High-speed phase- and group-delay scanning with a grating-based phase control delay line," *Opt. Lett.* **22**, 1811–1813 (1997).
7. E. B. Treacy, "Optical pulse compression with diffraction gratings," *IEEE J. Quantum Electron.* **QE-5**, 454–458 (1969).
8. O. E. Martinez, J. P. Gordon, and R. L. Fork, "Negative group-velocity dispersion using refraction," *J. Opt. Soc. Am. A* **1**, 1003–1006 (1984).
9. A. M. Weiner, J. P. Heritage, and E. M. Kirschner, "High-resolution femtosecond pulse shaping," *J. Opt. Soc. Am. B* **5**, 1563–1572 (1988).
10. J. X. Tull, M. A. Dugan, and W. S. Warren, "High-resolution, ultrafast laser pulse shaping and its applications," *Adv. Magn. Opt. Reson.* **20**, 1–65 (1997).
11. A. M. Weiner, D. E. Leaird, J. S. Patel, and J. R. Wullert, "Programmable femtosecond pulse shaping by use of a multielement liquid-crystal phase modulator," *Opt. Lett.* **15**, 326–328 (1990).
12. K. K. M. B. D. Silva, A. V. Zvyagin, and D. D. Sampson, "Extended range, rapid scanning optical delay line for biomedical interferometric imaging," *Electron. Lett.* **35**, 1404–1406 (1999).
13. Y. Zhao, Z. Chen, C. Saxer, S. Xiang, J. F. de Boer, and J. S. Nelson, "Phase-resolved optical coherence tomography and Doppler tomography for imaging blood flow in human skin with fast scanning speed and high velocity sensitivity," *Opt. Lett.* **25**, 114–116 (2000).
14. W. G. Yang, D. Keusters, D. Goswami, and W. S. Warren, "Rapid ultrafine-tunable optical delay line at the 1.55-mm wavelength," *Opt. Lett.* **23**, 1843–1845 (1998).
15. G. D. Love, "The unbounded nature of geometrical and dynamical phases in polarization optics," *Opt. Commun.* **131**, 237–240 (1996).
16. A. V. Zvyagin and D. D. Sampson, "Achromatic optical phase shifter–modulator," *Opt. Lett.* **26**, 187–189 (2001).
17. M. Stern, J. P. Heritage, and E. W. Chase, "Grating compensation of third-order fiber dispersion," *IEEE J. Quantum Electron.* **28**, 2742–2748 (1992).
18. L. Deck and P. de Groot, "High-speed noncontact profiler based on scanning white-light interferometry," *Appl. Opt.* **33**, 7334–7338 (1994).
19. E. D. J. Smith, A. V. Zvyagin, and D. D. Sampson, "Real-time dispersion compensation in scanning interferometry," *Opt. Lett.* **27**, 1998–2000 (2002).
20. F. Toigo, A. Marvin, V. Celli, and N. R. Hill, "Optical properties of rough surfaces: general theory and the small roughness limit," *Phys. Rev. B* **15**, 5618–5626 (1977).
21. G. S. Agarwal, "Interaction of electromagnetic waves at rough dielectric surfaces," *Phys. Rev. B* **15**, 2371–2383 (1977).